

Magnetic field configurations in neutron stars from MHD simulations

Ankan Sur¹*, Brynmor Haskell¹, Emily Kuhn²

¹*Nicolaus Copernicus Astronomical Center, Polish Academy of Sciences, Bartycka 18, 00-716 Warsaw, Poland*

²*Department of Physics, Yale University, New Haven, CT 06520, United States*

Last updated 21 December 2024; in original form 21 December 2024

ABSTRACT

We have studied numerically the evolution of magnetic fields in barotropic neutron stars, by performing nonlinear magnetohydrodynamical simulations with the code PLUTO. For both initially predominantly poloidal and toroidal fields, with varying strengths, we find that the field settles down to a mixed poloidal-toroidal configuration, where the toroidal component contributes between 10% and 20% of the total magnetic energy. This is, however, not a strict equilibrium, as the instability leads to the development of turbulence, which in turn gives rise to an inverse helicity cascade, which determines the final “twisted torus” setup. The final field configuration is thus dictated by the non-linear saturation of the instability, and not stationary. The average energy of the poloidal and toroidal components, however, is approximately stable in our simulations, and a complex multipolar structure emerges at the surface, while the magnetic field is dipolar at the exterior boundary, outside the star.

Key words: stars: neutron, magnetic field; methods: numerical; magnetohydrodynamics (MHD), instabilities, turbulence

1 INTRODUCTION

Neutron star(s) (NS(s)) are extremely dense compact objects bearing the strongest magnetic fields known to date in the universe. The surface field strength for ordinary NSs ranges from $10^{12} - 10^{13}$ G while for magnetars, it goes well beyond 10^{15} G. Despite such estimates for the strength of the magnetic field, its structure is not completely known to us. Polarimetric studies of radio emission from pulsars have been used to probe the geometry of pulsar magnetospheres. Such observations favour a predominantly dipolar magnetic field, although there is evidence for higher multipoles (Chung & Melatos 2011a,b; de Lima et al. 2020). Recent observations in X-rays by the NICER mission have confirmed that the field at the surface is far from an aligned dipole, but rather an intricate multipolar structure is present (Bilous et al. 2019).

The internal field topology is even more difficult to probe directly with observations, but is thought to play a fundamental role in determining the nature and strength of electromagnetic and gravitational wave emission of the star (Thompson & Duncan 1996; Cutler 2002; Güver et al. 2011). As the field of gravitational wave astronomy advances, it may, in fact, be possible to use gravitational-wave signatures to discriminate between different magnetic field topologies (Lasky & Melatos 2013). It is thus of great importance to obtain a theoretical understanding of the interior field and use numerical simulations to explore its nature.

Several studies have been carried out to investigate the equilibrium configuration of magnetic main sequence stars and white dwarfs, in which the Lorentz force is balanced by pressure and gravity; e.g. for the axisymmetric case by Braithwaite & Spruit (2006); Braithwaite & Nordlund (2006); Braithwaite (2007); Aramaza et al. (2015) and a similar non-axisymmetric study by Braithwaite (2008). For the NS case, equilibrium solutions in Newtonian gravity were obtained by Haskell et al. (2008); Lander & Jones (2009); Lander et al. (2010); Lander & Jones (2011); Herbrik & Kokkotas (2017); Frederick et al. (2020) and in general relativity by Kiuchi & Yoshida (2008); Ciolfi et al. (2010); Ciolfi & Rezzolla (2013) and the role of stratification was investigated by Glampedakis et al. (2012); Reisenegger (2009). Finding equilibrium and stability conditions for the magnetic field in stars has been an important long-standing question that dates back to earlier studies by Chandrasekhar & Fermi (1953); Tayler (1957); Tayler (1973); Wright (1973); Markey & Tayler (1973, 1974); Flowers & Ruderman (1977). A purely poloidal field undergoes the so-called “Taylor instability” and is thus unstable (Ferraro 1954; Monaghan 1965; Bocquet et al. 1995). In NSs this instability has been studied numerically in general relativity by Ciolfi et al. (2011); Lasky et al. (2011); Ciolfi & Rezzolla (2012), who confirm that an initially poloidal field is unstable on the order of an Alfvén crossing timescale and toroidal components of the field are generated. The equilibrium configuration is often approximated as a *twisted-torus* configuration where a toroidal component stabilises the poloidal field (Braithwaite & Nordlund 2006; Braithwaite 2007) or a *tilted-*

* Contact e-mail: ankansur@camk.edu.pl

torus configuration with the magnetic axis tilted with respect to the rotation axis (Lasky & Melatos 2013), as the inclination angle between the two grows (Lander & Jones 2018, 2019). An initial purely toroidal field is also unstable to the azimuthal wavenumber $m=1$ mode of oscillation which is independent of the field strength but instead depends on the geometry (Roxburgh 1966; Tayler 1973) and can lead to strong poloidal components developing.

Several open questions remain, however, as to the exact configuration the field will settle down to. Specifically, while it is clear that a mixed field is required for stability, the relative strength of the components cannot be obtained directly from the study of equilibrium configurations which generally allow a degree of freedom in tuning this parameter (see Glampedakis & Lasky 2016 for an in depth discussion of this issue). It is thus possible to obtain models in which the toroidal field strength ranges from a few percent of (Lander & Jones 2009) to more than an order of magnitude higher (Cioffi & Rezzolla 2013) than the strength of the poloidal component.

In fact, the stability of barotropic stars has been questioned by Lander & Jones (2012); Mitchell et al. (2015) who hypothesize that all barotropic models are unstable, while Reisenegger (2009); Akgün et al. (2013) suggest that stratification plays an important role in stabilising the field, and non-barotropic models of magnetised stars are stable. Since most hydromagnetic instability studies have focused on building equilibrium configurations starting with a specific choice of geometry, fully non-linear time evolutions for NSs for a range of initial topologies and a barotropic EOS need to be carried out, to determine not only whether the field is unstable, but also, crucially, what the final state determined by the non-linear saturation of the instability is. It is also important to understand how magnetic helicity is generated and transferred in the star as the instability proceeds. NS interiors are expected to be turbulent and the evolution of the field, especially soon after birth when the star is still differentially rotating, is likely linked to the action of a dynamo in the interior (Thompson & Duncan 1993).

It is crucial to obtain an understanding of these issues, as the field configuration of a NS plays an important role in attempts to determine the mass and radius of the star from X-ray observations (Riley et al. 2019; Miller et al. 2019), and in determining the gravitational wave emission properties of the system (Lasky 2015).

To address the problem in this paper we perform non-linear magnetohydrodynamical (MHD) simulations of magnetised NSs to characterize the instability, the global evolution, and the final configuration of the magnetic field. We work in Newtonian gravity as general relativity generally does not affect the qualitative nature of the magnetic instabilities (Siegel et al. 2013), and this allows us to explore a larger portion of parameter space. We explore different setups, both in resistive and ideal MHD, and different initial conditions, which allow for fields with initially stronger poloidal or toroidal components. The initial field generally goes unstable on an Alfvén crossing timescale and we follow the development of the instability, which leads to the development of turbulence in the system, which in turn seeds the growth of magnetic helicity.

Our results show that in general the system reaches turbulent equilibrium, in which the average field strengths settle down to a stable ratio. In all our final field configurations, including those with initially stronger toroidal fields, the field is predominantly poloidal, but a weaker toroidal component ($\lesssim 20\%$ of the total magnetic energy) is present.

The article is arranged as follows: In section 2, we discuss our numerical setup; In section 3, we discuss our results for the different setups considered in our simulations; section 4 discusses the effect

of resistivity and section 5 the onset of turbulence. The convergence of our results is discussed in section 6, and finally conclusions and discussions are presented in section 7.

2 PHYSICAL SYSTEM AND NUMERICAL SETUP

We use the publicly available code PLUTO ¹ by Mignone et al. (2007) to solve the MHD equations [1-4].

$$\frac{\partial \rho}{\partial t} + \nabla \cdot (\rho \mathbf{v}) = 0 \quad (1)$$

$$\frac{\partial \mathbf{v}}{\partial t} + \mathbf{v} \cdot \nabla \mathbf{v} + \frac{1}{\rho} \mathbf{B} \times (\nabla \times \mathbf{B}) + \frac{1}{\rho} \nabla p = -\nabla \Phi \quad (2)$$

$$\frac{\partial \mathbf{B}}{\partial t} + \mathbf{B}(\nabla \cdot \mathbf{v}) - (\mathbf{B} \cdot \nabla) \mathbf{v} + (\mathbf{v} \cdot \nabla) \mathbf{B} = 0 \quad (3)$$

$$\frac{\partial p}{\partial t} + \mathbf{v} \cdot \nabla p + \rho c_s^2 \nabla \cdot \mathbf{v} = 0, \quad (4)$$

where c_s is the sound speed. The above set of equations are closed with a barotropic EOS given by $p = p(\rho)$, which we take to be an $n = 1$ polytrope. Although, the initial parameters are defined in terms of primitive variables $(\rho, \rho, \mathbf{v}, \mathbf{B})$, computations are done using conservative variables $(\rho, \rho \mathbf{v}, E, \mathbf{B})$, where $E = \rho \epsilon + \rho \mathbf{v}^2/2 + \mathbf{B}^2/2$. Equations [1-4] are solved in a spherical coordinate system in 3 dimensions using a static grid which is divided into a number of points with N_r in the radial direction r , N_θ in the polar direction θ , and N_ϕ in the azimuthal direction ϕ . However, our r -grid is non-uniform having a resolution ($\Delta r \sim 0.19$ km) inside the star as compared to the atmosphere (where $\Delta r \sim 0.25$ km). Interpolations are done with a piece-wise parabolic function which is accurate to second order in time. A Runge Kutta 3 (RK3) time stepping is used and we set the Courant-Friedrichs-Lowy (CFL) limit to 0.3. We use a Harten-Lax-van Leer (HLL) Riemann solver for computing the fluxes. The solenoidal constraint $\nabla \cdot \mathbf{B} = 0$ is maintained using the hyperbolic divergence cleaning method. The code does not solve the Poisson equation. We analytically solve for the gravitational potential in different regions of the star and provide it as an input. Our gravitational field does therefore not evolve with time. The density distribution of the star is, however, only very weakly affected by the magnetic field and this is generally a good approximation (Haskell et al. 2008).

2.1 Initial Conditions

We consider a non-rotating star which is modeled by solving the Lane-Emden equation with $n = 1$ polytrope such that ² $P = k_\star \rho^2$, where $k_\star = 4.25 \times 10^4 \text{ gm}^{-1} \text{ cm}^{-5} \text{ s}^{-2}$ ³. We choose a background star with a total mass of $1.4M_\odot$, radius $R_\star = 10$ km and central

¹ <http://plutocode.ph.unito.it/>

² PLUTO does not have an inbuilt barotropic EOS. We have suitably modified the ISOTHERMAL EOS such that the proportionality constant k_\star remains fixed.

³ All our work is carried out using CGS units.

density $\rho_c = 2.17 \times 10^{15}$ gm cm⁻³. The density of the star only has radial dependence given by,

$$\rho = \rho_c \frac{\sin y}{y} \quad (5)$$

where $y = \frac{\pi r}{R_\star}$. As in most numerical MHD studies, it is necessary to replace the vacuum outside the stellar surface with an atmosphere of low-density fluid, in order to avoid computational difficulties due to diverging Alfvén velocities as the density falls to zero. Equation 5 shows that ρ falls rapidly and vanishes while approaching the edge of the star. Since the atmosphere has a non-zero density ρ_{atm} , this would cause a sharp gradient across the boundary of the star. In order to prevent such unrealistic jumps in density at the surface, we cut the star at a radius of $r = 0.975R_\star$ so that $\rho(r \leq R) > \rho_{\text{atm}}$. We set $\rho_{\text{atm}} = 10^{12}$ gm cm⁻³ and explore two different setups, one in which the atmosphere extends up to a distance of $1.2 R_\star$ with no resistivity while another which extends up to $2R_\star$ and includes a resistive layer in the atmosphere of the star, which we will discuss in detail in the following sections. We start our simulation with two different initial conditions. The first is obtained by introducing a purely poloidal field (Haskell et al. 2008),

$$B_r = \frac{B_p \cos \theta}{\pi(\pi^2 - 6)} [y^3 + 3(y^2 - 2) \sin y + 6y \cos y] \quad (6)$$

$$B_\theta = \frac{B_p \sin \theta}{2\pi(\pi^2 - 6)} [-2y^3 + 3(y^2 - 2)(\sin y - y \cos y)] \quad (7)$$

$$B_\phi = 0.0 \quad (8)$$

inside the star and

$$B_r = \frac{B_p R^3 \cos \theta}{r^3} \quad (9)$$

$$B_\theta = \frac{B_p R^3 \sin \theta}{2r^3} \quad (10)$$

$$B_\phi = 0 \quad (11)$$

outside the star, where B_p is the surface poloidal magnetic field strength, which we set to be $B_p = 10^{17}$ G. Such a strong magnetic field reduces the timescales allowing us to explore greater possibilities within a shorter run of the simulation. To accelerate the development of the instability, we add a small perturbation to the velocity of the fluid elements located along the neutral line (where the poloidal field vanishes), given by

$$v_\theta = \sqrt{\frac{15}{8\pi}} \sin \theta \sin 2\phi \quad (12)$$

$$v_\phi = \sqrt{\frac{15}{8\pi}} \sin \theta \sin 2\phi \cos \theta \quad (13)$$

We confirm that this has no other effects apart from triggering the instability which still grows but takes longer to develop without the perturbation. Additionally, we also test another initial condition, with the same poloidal field, but a stronger toroidal component ($B_t = 2 \times 10^{17}$) inside the star given by

$$B_\phi = B_t \frac{\sin y \sin \phi}{\pi}, \quad (14)$$

and study its evolution with time.

2.2 Timescales

The two important timescales in our simulation are the sound crossing time (τ_{cs}) and the Alfvén time (τ_A). τ_A is defined by

$$\tau_A = \frac{2R_\star \sqrt{4\pi \langle \rho \rangle}}{\langle B \rangle} \quad (15)$$

where, $\langle \dots \rangle$ represent volume averaged quantities. The field evolution depends on the Alfvén timescale while the hydrostatic equilibrium depends on the shorter sound crossing time. Our high surface magnetic field strength assures that $\tau_{cs} \ll \tau_A$ and as such the dynamics are independent of the sound crossing time. The Alfvén time is not a constant throughout the entire run of the simulation, instead it varies with the change in magnetic field. Initially, the magnetic field rearranges and its density becomes higher in the core of the star. Thus, τ_A changes in subsequent times and does not remain constant. In our simulations with $B_p = 1 \times 10^{17}$ G, we obtain an average $\tau_A = 1.3$ ms.

2.3 Boundary Conditions

Our objective is to understand the interior field strength and configuration of a NS if the exterior dipolar field has a given strength, inferred from observations. With this physical picture in mind, we set the exterior boundary condition of our simulation by fixing the magnetic field to be poloidal in the r and the θ directions maintaining the same gradient of the field, while we use periodic boundaries along the ϕ direction. The velocities are all set to zero at the boundaries. Note that to correspond to the physical prescription described above, the exterior boundary should be far from the star, where the dipolar component provides the dominant contribution to the spin-down torque. Due to numerical limitations we are far more restricted and, in practice, have to place our exterior boundary close to the star. As already mentioned we have studied two setups, with the exterior boundary at $1.2 R_\star$ and another which extends up to $2R_\star$. We find that our results do not depend significantly on the location of the outer boundary. Extending the atmosphere farther out, in regions where higher multipoles of the field fall off much more rapidly than the dipolar component, will, thus not alter our conclusions.

At the inner boundary in the radial direction, we set the density of the star to follow the profile given by equation 5 while at the outer boundary we set the density to be ρ_{atm} .

3 RESULTS

We now move on to discuss the results of our simulations. In this section we will first present the results of our non-resistive setup, and then discuss all the results corresponding to the resistive atmosphere, in detail, in section 4. Nevertheless the main conclusions are not affected by the choice of setup. All setups, both resistive and non-resistive, are initially unstable, independently of whether we choose a purely poloidal field as initial condition or a twisted torus with a stronger toroidal component. In all cases we find that turbulence develops and the field settles to a state which is not strictly an equilibrium, but in which the non-linear saturation of the instability determines a stable average of the field strengths, such that the energy of the toroidal component is roughly 10 – 20% of the total magnetic energy.

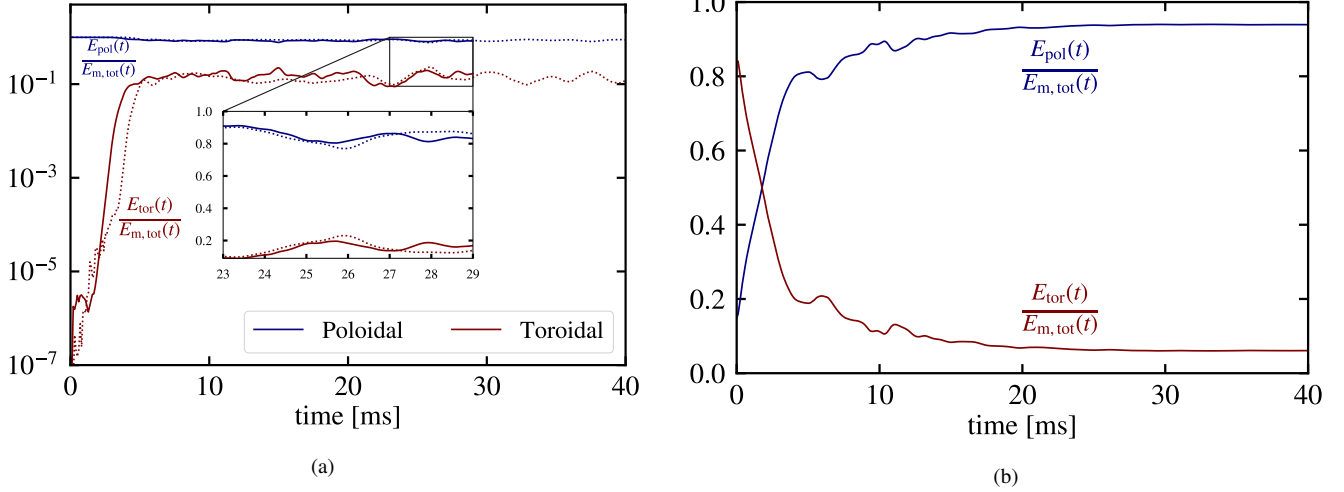


Figure 1. (a) A comparison of the poloidal (E_{pol}) and toroidal (E_{tor}) field energies normalized by the total magnetic field energy $E_{\text{m,tot}}$ at each time t for our model with $\{B_p = 10^{17} \text{ G}, B_t = 0\}$. The atmosphere extends up to 12 km (represented by solid lines), whereas the dotted lines represent a model with an extended atmosphere till 16 km. The inset in the figure shows a linear scale comparison between the two components. (b) Evolution of the field energies starting with an initially stronger toroidal field with $\{B_p = 10^{17} \text{ G}, B_t = 2 \times 10^{17} \text{ G}\}$. We find $E_{\text{tor}} \leq 20\% E_{\text{m,tot}}$ in both the cases.

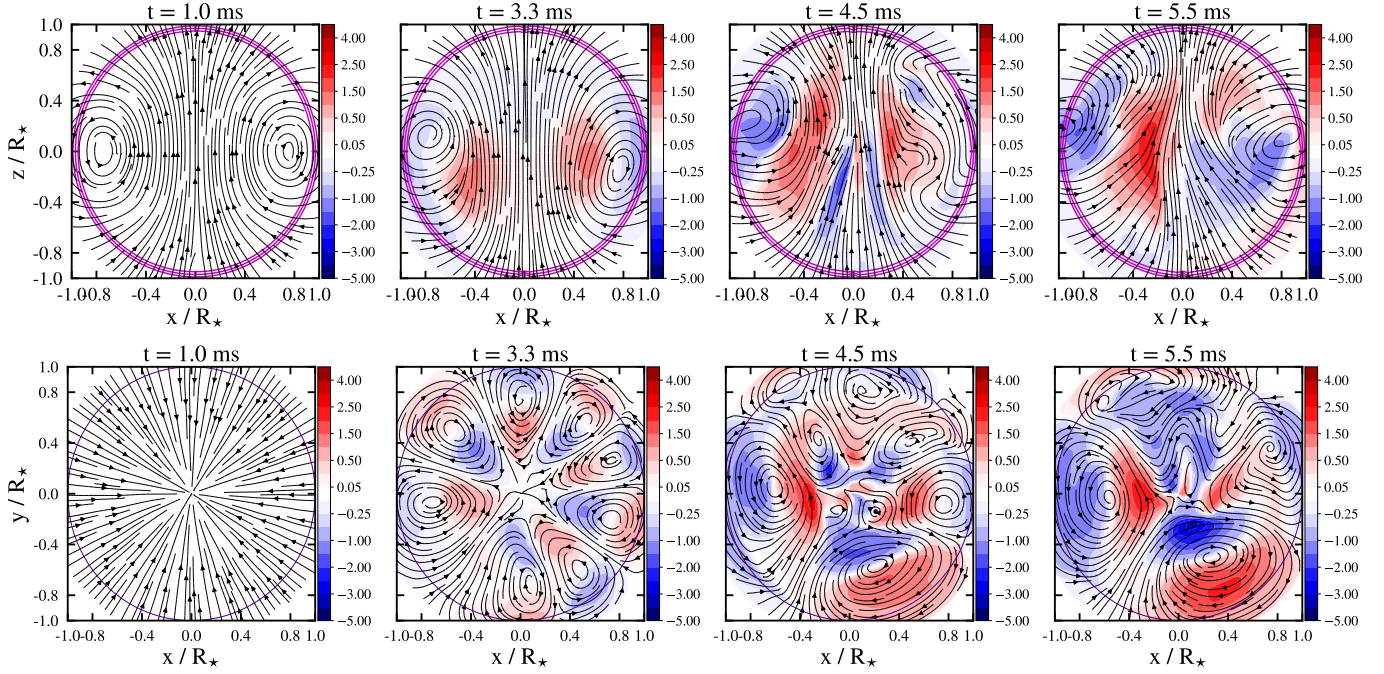


Figure 2. Snapshots of the star from meridional view (top) and equatorial view (bottom) showing the development of a toroidal field (color scale indicates strength of B_ϕ normalized by $2 \times 10^{16} \text{ G}$). In the top row, the purple lines show equidensity contours $\rho \in (10^{13}, 5 \times 10^{13}, 10^{14}) \text{ gm cm}^{-3}$. The streamlines shown are the poloidal fieldlines that thread through the main body of the star. In the bottom row, the streamlines show the toroidal fieldlines and the violet contour shows the location of R_\star . Times of the snapshots are given as figure titles.

3.1 Field Configurations and Strengths

Let us analyse in detail the evolution of the relative strengths of the poloidal and toroidal field components for our non-resistive setup. Figure 1a shows the evolution of poloidal and the toroidal magnetic field energies normalized by the total magnetic field energy at each time for the entire run of a simulation in which the initial condition was a purely poloidal field. The toroidal component initially gains strength from the initial perturbation we gave. After 3 ms, the poloidal field becomes unstable and the toroidal compo-

ment undergoes an exponential growth with its strength becoming comparable to the poloidal component. This period of exponential growth corresponds to 1 Alfvén crossing time during which the toroidal component fully develops close to the neutral line. After $t = 5$ ms, the field reaches pseudo-equilibrium and the evolution becomes less dramatic. However, the toroidal part remains weaker ($\leq 20\%$ of the total magnetic energy) than its poloidal counterpart. Even with a mixed-field initial condition with a stronger toroidal component ($B_t = 2 \times 10^{17} \text{ G}$ as compared to a poloidal strength of

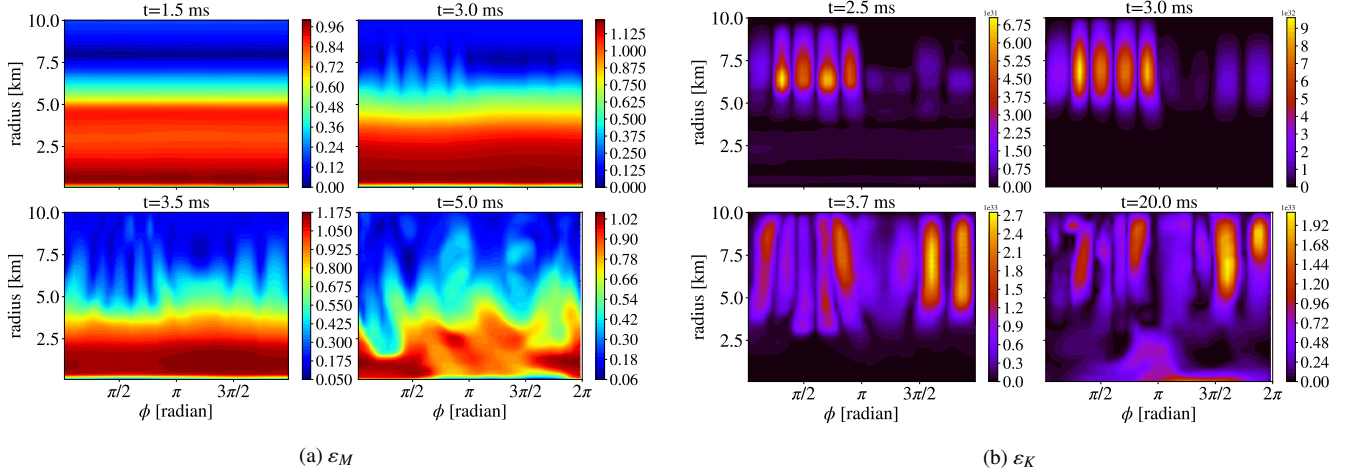


Figure 3. Energy densities plotted in the equatorial plane of the star, i.e. at $\theta = 90^\circ$ for different times t in our simulation. At $t = 3$ ms, we see that the neutral line gets disrupted showing the formation of a strong toroidal component.

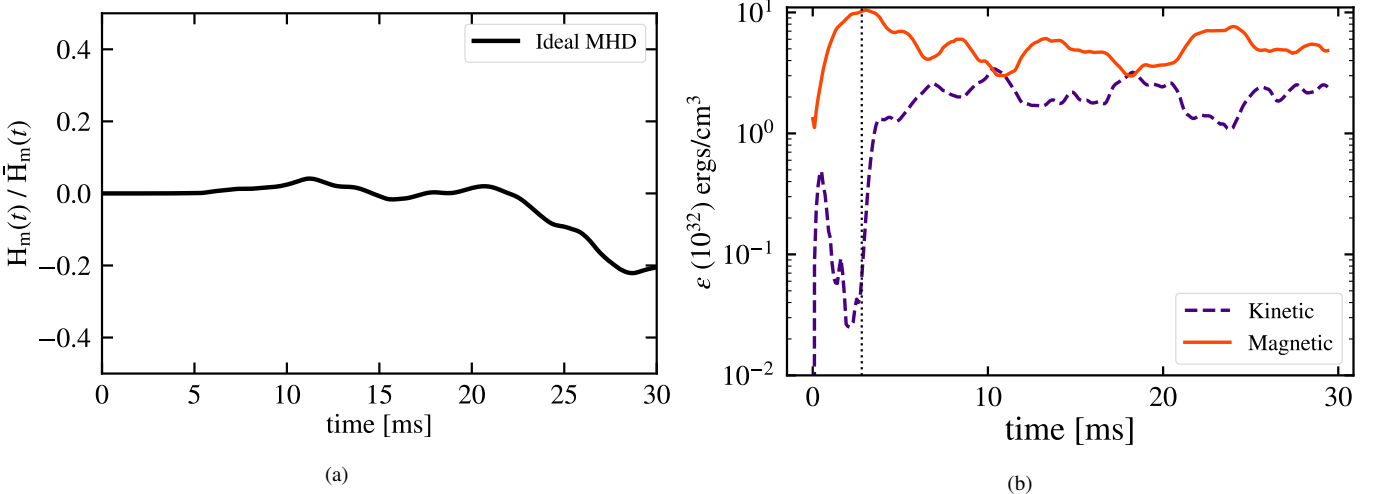


Figure 4. (a) Time evolution of the magnetic helicity for ideal-MHD setup (i.e. resistivity $\eta_0 = 0$). (b) Average magnetic field energy density (ε_M) and the average kinetic energy density (ε_K) normalized by 10^{32} ergs/cm³ plotted as a function of time. After an initial transient, the onset of instability is seen at $t = 3$ ms (represented by the dotted line) when there is a sharp rise in the kinetic energy of the system.

$B_p = 10^{17}$ G), we see that the final configuration settles to a weaker toroidal field as compared to the poloidal field (see figure 1b).

Figure 2 shows snapshots of the formation of the toroidal component in the meridional (x-z) plane and the equatorial (x-y) plane, for an initially poloidal field. The colors show the strength of B_ϕ only. The region inside the star, where the fieldlines close, moves in and out during the initial stage when the fluid starts readjusting to the changing magnetic field. The null line seems to move outwards during the evolution. As pointed out by Glampedakis & Lasky (2015), closed fieldlines in the core of the star cause it to be magnetically decoupled with the rest of the star by developing a velocity lag between these regions. During the initial stage, the field can be treated as a linear perturbation on top of a stationary background field. The nonlinear terms start to dominate after the onset of the ‘kink’-instability at $t \sim 3$ ms. The dynamics thereafter change rapidly, breaking the axisymmetry and the field inside the star attains a complex geometry with the mixed-field configuration. The toroidal component creates vortex-like structures (shown in the lower-panel of figure 2) in order to conserve the magnetic

helicity (Ciolfi et al. 2011) which is initially zero due to our choice of a purely poloidal field as initial condition. These structures show higher-order modes (see figure 2 at $t = 3.3$ ms) which are replaced by lower-order modes at later stages during the evolution. The presence of the kink-instability is visible in our simulation in figure 3a, where the absolute value of the magnetic field strength is plotted on the equatorial plane of the star. The deep blue line feature at $r \sim 8$ km at $t = 1.5$ ms shows the location of the neutral line. This gets distorted and small lumps are seen at $t = 3$ ms which evaporate thereafter. Similarly, we plot the kinetic energy of the star on the equatorial plane (figure 3b) and note the different modes of oscillations present in our simulation. Higher order modes are visible at $t = 2.5$ ms, and start coupling with each other at later stages as seen at $t = 20$ ms.

The magnetic helicity H_m measures the amount of ‘twist’ in the magnetic field and is given by:

$$H_m = \int_V \mathbf{A} \cdot \mathbf{B} dV \quad (16)$$

where \mathbf{A} is the magnetic vector potential. The helicity in equation

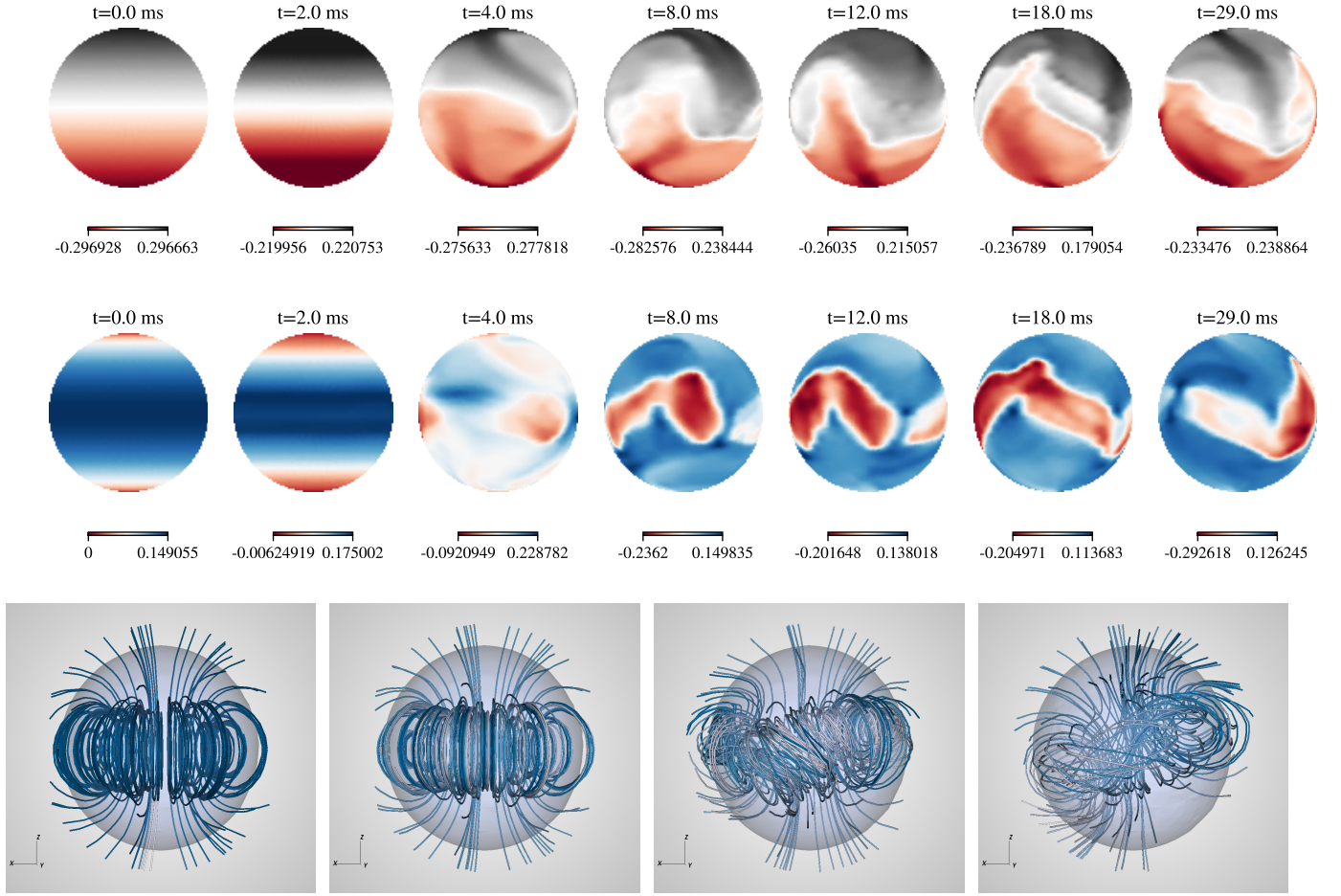


Figure 5. Surface distribution of B_r (top) and B_θ (middle) at various times t , given as figure titles. The colorscale (normalized by 10^{17} G) shows the strength of the field. (bottom) 3-D visualization of the magnetic field configuration at times $t=0$ ms, $t=3$ ms, $t=10$ ms and $t=20$ ms (from left to right).

(16) is a conserved quantity in ideal MHD, with a non-zero value generally linked to non-ideal effects such as reconnections. Figure 4a shows the time evolution of the quantity H_m/\bar{H}_m , where the magnetic helicity is normalized by $\bar{H}_m = 0.5 \times E_{m,\text{tot}} \times 0.8R_\star$, where $E_{m,\text{tot}}$ is the volume integrated total magnetic energy. We remark that the choice of gauge for \mathbf{A} is irrelevant in this case. Initially, the helicity remains zero until there is axisymmetry in our simulation. However, as the star tries to reach an equilibrium, the helicity becomes non-zero.

We will see in detail section 5 that this is linked to the development of turbulence, in which following the initial development of kinetic helicity after the instability, an inverse cascade takes helicity from the resistive small scales to larger scales. This is expected as the system attempts to conserve helicity by transferring it from the small scale turbulent field to the larger scale field, thus moving it further from the resistive scale (Biskamp (2003)).

The atmosphere also plays a role in governing the internal dynamics of the field. We explore its effect by running simulations with different values of ρ_{atm} and find that an atmosphere with higher-density fluid (which allows the star to lose more magnetic energy) causes a relatively weaker toroidal field as compared to an atmosphere with lower-density fluid. Extending the atmosphere up to a larger distance also does not influence much the overall growth of field-energies. This is shown as dotted lines in figure 1a. As the influence of higher order multipoles is stronger close to the surface,

the fact that the results are mostly unaffected by the position of the boundary within a few stellar radii gives us a degree of confidence that these are a good approximation to the physically realistic situation, in which the dipolar field component is inferred further out at the light cylinder.

Figure 4b shows the variation of the volume averaged magnetic energy density ($\varepsilon_M = (B_r^2 + B_\theta^2 + B_\phi^2)/8\pi$) and the volume averaged kinetic energy density ($\varepsilon_K = \rho(v_r^2 + v_\theta^2 + v_\phi^2)/2$) with time. A peculiar feature of our evolutions is the initial rearrangement of the poloidal field, due to our choice of initial condition in which the field is stronger in the outer core. This leads to a rapid initial readjustment which takes it to a more stable configuration in which stronger near the center of the star and weaker in the exterior regions. As a consequence at $t \sim 1$ ms, there is a small peak in ε_K which the fluid gains in response to the initial readjustment of the magnetic field. Furthermore when we take a volume average of the field, this rearrangement is visible as a sudden rise in ε_M , as the field becomes stronger in the interior region over which we integrate. This can be seen in the first few milliseconds (figure 4b). Following this initial transient the field settles down, until it is affected by the onset of the ‘‘kink’’ instability at $t = 3$ ms (after ~ 1 Alfvén crossing time) when the magnetic energy falls and the kinetic energy rises sharply. This is ascribed to the conversion of magnetic energy to kinetic energy (see also Lasky et al. (2012)). Finally we note that the presence of the varicose mode, in which the flux tube near the

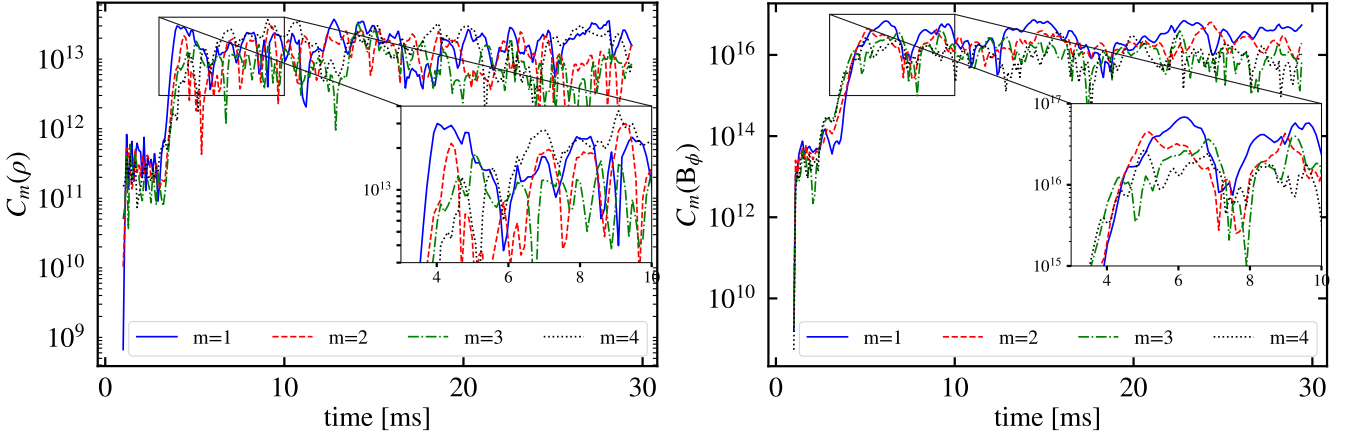


Figure 6. Fourier decomposition of ρ (left) and B_ϕ (right) into different azimuthal modes $m \in (1, 2, 3, 4)$ as a function of time for $B_p = 10^{17}$ G. The inset shows that the lower order modes for ρ grow faster compared to the higher order modes however the reverse is observed for B_ϕ where the higher order modes grow faster. An exponential growth is seen in both the quantities which saturates after few Alfvén crossing times when the star attains a pseudo-equilibrium state.

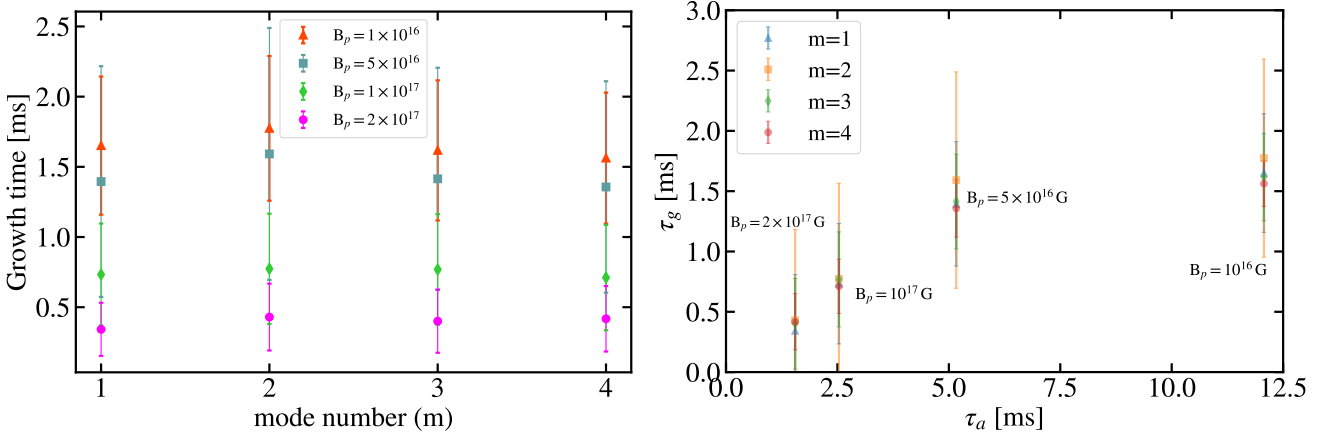


Figure 7. (left) shows the growth times for different modes with varying surface magnetic field strengths. (right) shows correlation between the growth times and the Alfvén crossing time. Our results are consistent with the expected linear relation between two quantities, but given that our error bars are large we do not present a fit to the data.

neutral line undergoes a change in cross-sectional area, is difficult to observe in 3D visualization of our simulation (see figure 5) because our Alfvén crossing time is small and the instability growth time is thus too rapid. However the kink-instability is somewhat visible at $t=3$ ms.

3.2 Growth Times

We Fourier decompose B_ϕ and ρ into different modes m and calculate the complex weighted averages as prescribed in Zink et al. (2007); Lasky et al. (2011) given by

$$C_m(f) = \int_0^{2\pi} f(\bar{\omega}, \phi, z=0) e^{im\phi} d\phi \quad (17)$$

where $\bar{\omega} = \sqrt{x^2 + y^2} = 0.8R_\star$ lies in the equatorial plane of the star, and $f \in (\rho, B_\phi)$. Since equation 17 results in a complex number, we take the modulus to obtain $C_m(f)$. Figure 6 shows the modal struc-

ture of the instability. All the different modes $m \in (1, 2, 3, 4)$ considered show the presence of the instability as each one grows exponentially by three-four orders of magnitude in one Alfvén crossing time before settling down to a pseudo-equilibrium state. For $C_m(\rho)$, visually, the lower-order modes grow faster, i.e. $m = 1$ mode grows faster than $m = 2$, and so on, whereas for B_ϕ , we see that the higher-order modes grow faster, i.e. $m = 3$ mode grows faster than $m = 2$, and so on.

Following Lasky et al. (2011), the instability growth time for a particular m during the exponential phase is defined by

$$\tau_g = \frac{\Delta t}{\Delta \ln[C_m(B_\phi)]} \quad (18)$$

Figure 7 shows the growth times for the different modes with varying surface magnetic field strength. In calculating equation 18, we do not adopt a single point, rather we take different realizations during the exponential phase and then calculate the mean and standard deviation of growth times. We find that the τ_g for the various

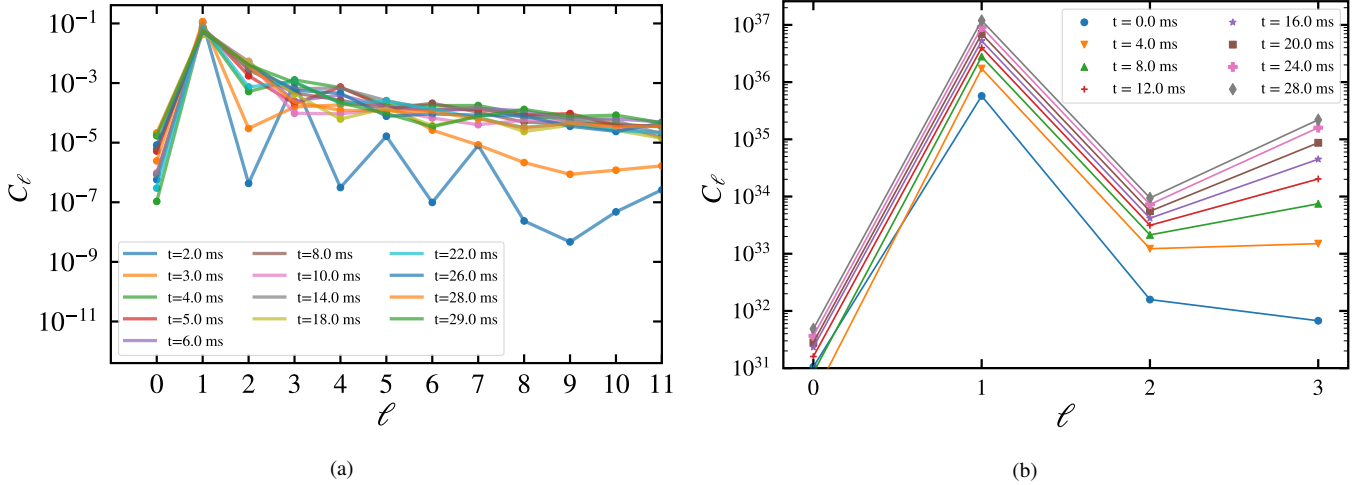


Figure 8. (a) Angular power spectrum for the scalar field B_r calculated at $r = R_\star$ plotted as a function of multipoles. (b) Power spectrum calculated for the magnetic field by decomposing it into vector spherical harmonics. The colors show different times in our simulation.

modes are not significantly different from each other unlike the prediction by Tayler (1957) where higher-order modes have a shorter growth time. It should be noted that our field strength B_p corresponds to a weaker $\langle B \rangle$ which is otherwise used in the literature to calculate τ_A . From figure 7, we find that the growth time scales approximately with the chosen range of magnetic field, although the large error bars do not allow to accurately test the scaling.

3.3 Power Spectrum

We use the `healpy` modules to calculate the angular power spectrum of B_r . Any scalar function defined on a sphere can be expanded into spherical harmonics. Given a map, the angular power spectrum is calculated using

$$C_\ell = \frac{1}{2\ell + 1} \sum_{m=-\ell}^{\ell} \langle |a_{\ell m}|^2 \rangle \quad (19)$$

where,

$$a_{\ell m} = \int d\mathbf{u} B(\mathbf{u}) Y_{\ell m}^*(\mathbf{u}) \quad (20)$$

$B(\mathbf{u})$ is a scalar field depending on the angular coordinates \mathbf{u} and $Y_{\ell m}^*$ is the complex conjugate of the spherical harmonics. Figure 8a shows that $\ell = 1$ contributes maximum to the total power in B_r , followed by $\ell = 2$ and $\ell = 4$ respectively. In figure 8b, we decomposed the magnetic field into vector spherical harmonics and calculated the power according to equation 19 for multipoles $\ell \in (0, 1, 2, 3)$. In this case, the $a_{\ell m}$'s were calculated using the definition of vector multipole moments (see for e.g. Barrera et al. (1985)). Initially, the field is dipolar. However, the higher-order multipoles gain power with time and the field structure becomes complex. This can be approximately seen in figure 5 where the field configuration evolves, and the neutral line migrates. We note, however, that the timescale on which this tilt occurs is dictated by numerical dissipation, and faster than would be expected in a realistic NS.

4 EFFECT OF RESISTIVITY

In the previous section we have considered a non-resistive setup in ideal-MHD, which reflects the expectation that the NS interior is a highly conductive medium. In practice, however, this approximation breaks down close to the surface of the NS as the density decreases, and resistive effects play an important role in the long term evolution of the magnetic field (for a recent review see Pons & Viganò 2019). As one moves further towards the exterior, a low density plasma is thought to surround the NS, in which now the tenuous fluid is tied to the magnetic field and the force-free approximation is generally used to understand the dynamics of the magnetosphere and the emission properties of the star (Goldreich & Julian 1969; Spitkovsky 2006; Philippov & Spitkovsky 2018).

In practice, most numerical studies of fields in NS interiors have approximated the exterior plasma in terms of an atmosphere with a resistivity, mostly to prevent shocks at the stellar boundary which otherwise lead to numerical instabilities. Although our non-resistive setup is stable for a dense enough atmosphere, we nonetheless explore the effects of resistivity on the simulation, in order to investigate if any substantial differences arise. We use a profile given by $\eta(r) = 0$ if $r < 0.9R_\star$, otherwise, $\eta(r) = \eta_0$ if $r \geq 0.9R_\star$, where η_0 is a constant.

The diffusion timescale, defined as $\tau_d = R_\star^2/\eta$, is larger than the Alfvén crossing time ($\tau_d \gg 10\tau_A$). We choose a value of η_0 such that this condition is satisfied. This leads us to the following relation $\eta_0 \leq R_\star \langle B \rangle / \sqrt{4\pi \langle \rho \rangle} = 10^{12} \text{ cm}^2 \text{s}^{-1}$. We set $\eta_0 = 10^8 \text{ cm}^2 \text{s}^{-1}$ in our simulation. The above choice of the profile maintains the ideal-MHD condition in the bulk of the star. We explore different values of $\eta_0 \in \{10^8, 10^{10}, 10^{12}\}$. Additionally, we extend our atmosphere up to 20 km ($= 2R_\star$). Figure 9a shows the long-term evolution of the poloidal and toroidal field energies (both normalized by the total magnetic field energy at each time) for a model with $\eta_0 = 10^8 \text{ cm}^2 \text{s}^{-1}$. Here again, we find that $E_{B_\phi} \leq 20\%$ of $E_{m,\text{tot}}$. The value of η_0 mostly modifies the timescales in our simulation as the onset of instability changes as illustrated in figure 9a

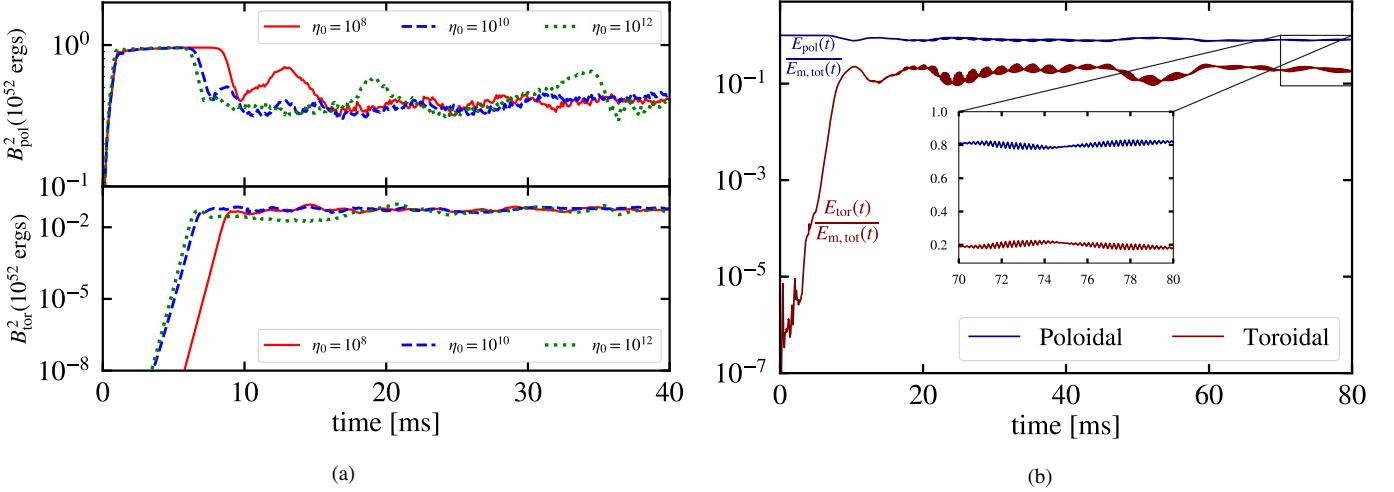


Figure 9. (a) Poloidal and Toroidal magnetic field energies as a function of time for three different values of η_0 . (b) Long-term evolution for the poloidal and toroidal field energies, normalized by the total magnetic energy, for the resistive atmosphere setup. The inline plot shows that $E_{\text{tor}} \sim 20\% E_{\text{m,tot}}$.

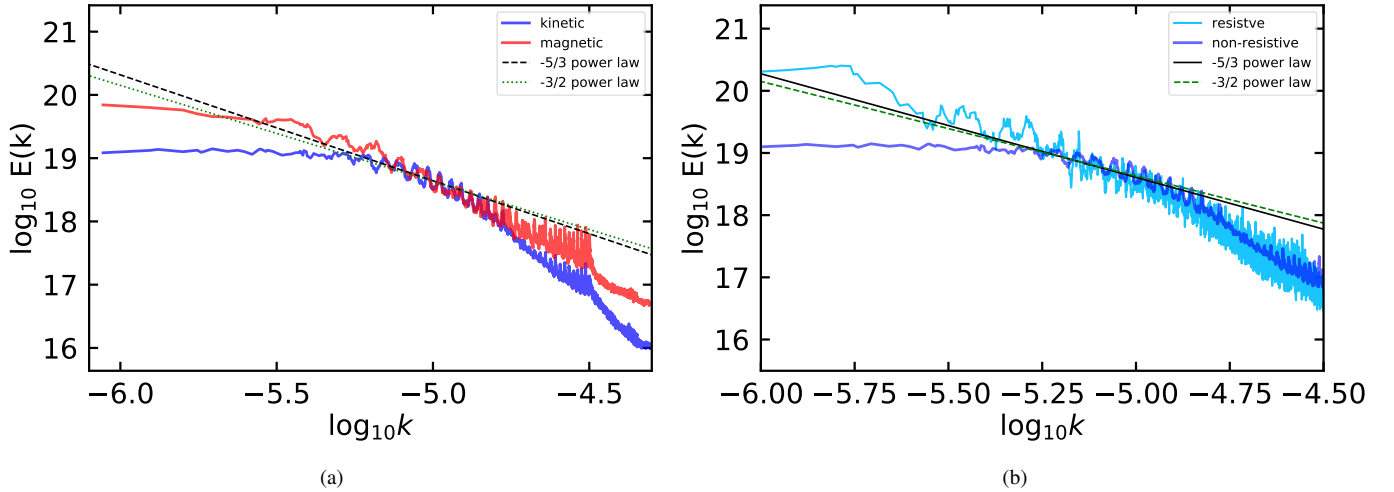


Figure 10. (a) Kinetic and magnetic energy spectra for our non-resistive setup. (b) A comparison of the kinetic energy spectrum between our resistive and non-resistive setups. In both the plots, the black dashed line shows $-5/3$ power law (Kolmogorov) while the green dotted line shows $-3/2$ power law (Iroshnikov-Kraichnan). We do not have a sufficiently high resolution to distinguish between the two spectra, but our results are consistent with a Kolmogorov spectrum, as found by previous MHD simulations, as described in the text.

5 TURBULENCE

The presence of turbulence which drives the evolution and properties of the systems in the presence of an embedded magnetic field is very prominent in astrophysics, e.g. in accretion disks, interstellar medium, stellar winds, etc. In fact X-ray observations reveal that the magnetic field of the sun is in a turbulent state (Lites et al. 2008), and one may thus expect a similar situation in a NS, in which a turbulent ‘equilibrium’ is reached, where average quantities can be studied, but in which the field is far from a stationary dipole.

Our simulations show that this is exactly what occurs: the non-linear saturation of the initial instabilities, lead, through the action of a small scale dynamo, to a turbulent mixed toroidal-poloidal field configuration, in which the ratio, averaged over the volume, of the energies in the two components reaches an equilibrium.

To quantify this statement we start by studying the distribution of kinetic energy over different length scales. We plot the spectra for the kinetic and magnetic energies as a function of wavenumbers

(k) in figure 10a. As expected, the system shows higher dissipation of energy for smaller scale eddies through viscosity. Thus, the dynamics inside the star is turbulent. The classical Kolmogorov theory (Kolmogorov (1941)) predicts that the turbulent energy spectrum in incompressible⁴ hydrodynamic turbulence follows $E(k) \propto k^{-5/3}$, where k is the modulus of the wave-vector ($k = \sqrt{k_x^2 + k_y^2 + k_z^2}$). In order to calculate the energy spectrum, we convert each velocity component into Cartesian space and Fourier transform them according to

$$\mathbf{u}(\mathbf{k}) = \iiint_{\mathbb{R}^3} \hat{\mathbf{u}}(\mathbf{x}) e^{i\mathbf{k} \cdot \mathbf{x}} d^3 x \quad (21)$$

⁴ Given the high speed of sound in NSs, we expect most eddies to be sub-sonic, and the effects of compressibility to be negligible.

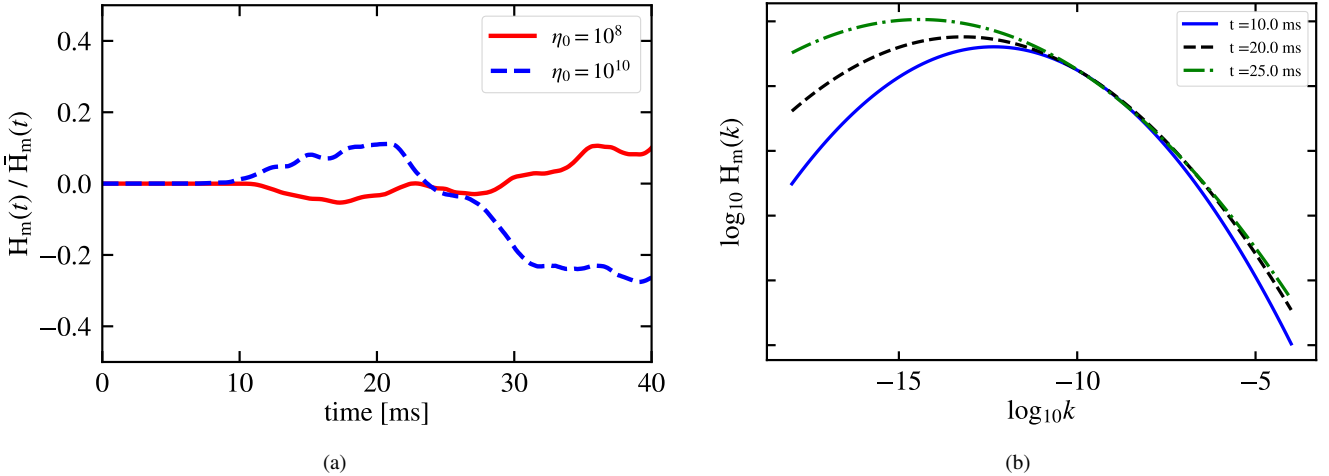


Figure 11. (a) Magnetic helicity plotted as a function of time for two different values of η_0 for a setup with $\tau_A \sim 10$ s. The helicity becomes nonzero as the instability sets in after one Alfvén crossing time. (b) The magnetic helicity spectrum at different times showing the phenomenon of an inverse cascade from the resistive small scales to larger scales.

In figure 10b, we plot the Kolmogorov spectrum for kinetic energy for our resistive setup. Our spectra are consistent with a Kolmogorov like dependence, however in MHD turbulence, where the main interaction happens within wave-packets moving with Alfvén velocities, the scaling relation follows $E(k) \propto k^{-3/2}$ (Iroshnikov (1964); Kraichnan (1965)). While previous numerical work has revealed the presence of a Kolmogorov spectrum also in MHD turbulence (Biskamp 2003), consistently with our interpretation, it is not possible to exclude $k = -3/2$ and determine the exact scaling relation with our limited resolution. Future high resolution studies are required to determine the exact nature of the turbulence in the NS problem. We note that the magnetic Reynolds number in MHD-turbulence is $R_m = Lv/\eta_0 = 10^6$, and since, $R_m \gg 1$, the magnetic field lines are advected with the fluid flow and diffusion is unimportant.

5.1 Cascade directions

As discussed before, the magnetic helicity (H_m) is an ideal MHD invariant and as such its spectral density is conserved in nonlinear interactions. Figure 11a shows the variation of H_m with time for two different values of η_0 . However, as turbulence is excited by the magnetic instabilities, H_m is created on the resistive scale on which non-ideal effects (dictated in our case by numerical resistivity) act, i.e. its value becomes non-zero, and it is scattered to different length scales. This transfer proceeds from larger to smaller wavenumbers showing an *inverse cascade* (Frisch et al. 1975), as the system attempts to conserve H_m by moving it to scales much larger than the resistive scale. With increasing time, the peak of the magnetic helicity spectrum shifts to smaller k showing the inverse cascade phenomenon, as seen in figure 11b.

This confirms the picture that turbulence plays a key role, by allowing to generate helicity in the system at small scales, and transfer it from the turbulent small scale structures to the larger scale magnetic field, thus creating a twisted-torus structure.

We note that at the end of our simulations turbulence has not decayed, but the average quantities, such as the average field strengths and magnetic energies have reached an equilibrium which is roughly constant over many Alfvén timescales.

6 CONVERGENCE

In this section, we present our convergence tests focusing in particular on the non-resistive setup. Figure 12a shows the variation in error of the total mass of the star with time and number of points in our grid respectively.

The mass of the star as a function of time was calculated assuming spherical symmetry. However, the poloidal field makes the star oblate and pushes material out which causes the loss of spherical symmetry. This effect is not taken into account in our calculation, as it is expected to deform the spherical profile of the star by less than $\approx 0.01\%$ for a field of $B = 10^{16}$ G (Haskell et al. 2008). In fact, we see that the highest resolution has the least error in the total mass. We find that the error reduces with an increase in the number of grid-points, and the mass determination appears to converge.

We also analyse the energy in the toroidal field, which is one of our key observables. In this case point-wise convergence is almost certainly lost, as turbulence develops. If the code is converging, we expect the difference in energies for our middle-lowest resolution setup (defined as “top”) to be higher than the difference in energies for the highest-middle resolution (defined as “bottom”). This is illustrated in figure 12b where $B = B_\phi$. Although, the plots are oscillating, the expected trend is seen, and at later times, when turbulence is fully developed, convergence is worse and at times lost.

As turbulence affects the dynamics of the field, and affects the convergence of our results, we use the spectrum of the turbulence itself as a diagnostic for convergence. We have already analysed the spectrum for our higher resolution simulations in the previous sections, and found it to be consistent with a Kolmogorov spectrum. In figures (13a) and (13b) we plot the kinetic energy spectrum for varying resolutions as a sanity check of the convergence of the code. As can be seen, the spectrum extends to smaller scales as expected, and is consistent with the scaling of

$$E(k) \propto k^{-5/3} \quad (22)$$

over a larger portion of parameter space, indicating that our higher resolution simulations are increasingly capturing the true dynamics of the system.

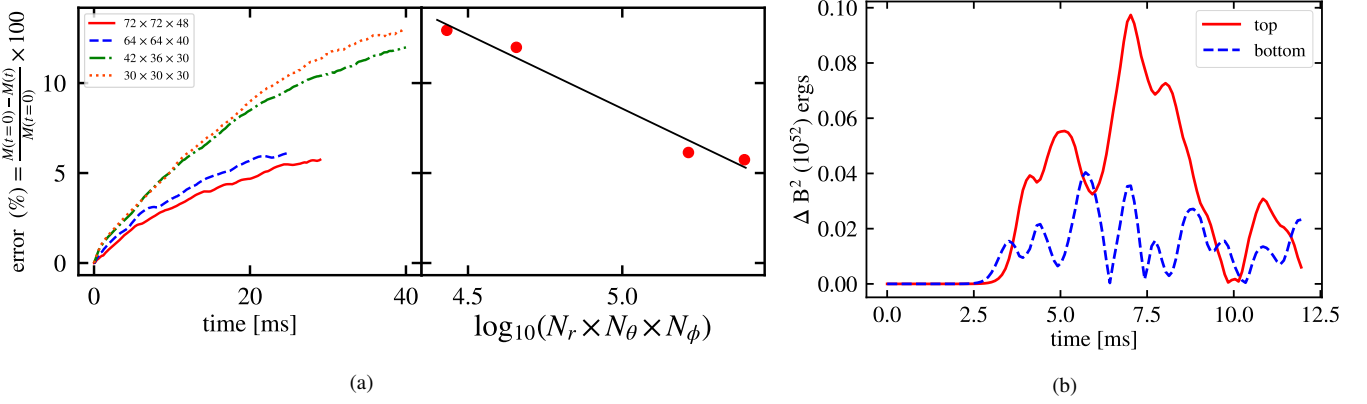


Figure 12. (a) Error in the total mass of the star as a function of (left) time, and (right) resolution for our purely poloidal setup with $B_p = 10^{17}$ G. The curves are incomplete for higher resolution setups as the simulation hit the wall clock time. (b) Difference in B_ϕ^2 plotted as a function of time. The red curve (top) shows the difference in energies between our setups with resolution $64 \times 64 \times 40$ and $30 \times 30 \times 30$. The blue curve (bottom) shows the difference in energies between our setups with resolution $72 \times 72 \times 48$ and $64 \times 64 \times 40$.

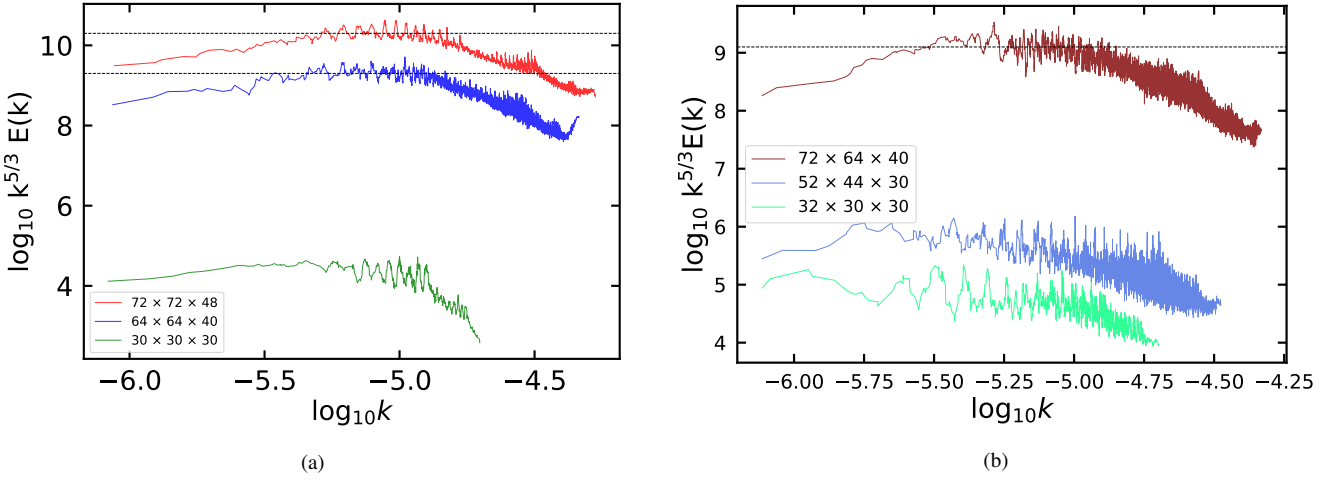


Figure 13. (a) Kolmogorov spectrum plotted for our non-resistive setup with varying resolution. According to Classical Kolmogorov theory, the spectrum follows $E(k) \propto k^{-5/3}$ in the inertial range, and deviate for high and low values of k where energy is injected and dissipated. We multiply $E(k)$ by $k^{5/3}$ and therefore expect to obtain a flat spectrum in the inertial range for the Kolmogorov case. This is seen in the region between $k = (10^{-5.25}, 10^{-4.9})$ for our highest resolution simulation (the black dotted lines are for reference). (b) Kolmogorov spectrum plotted for different resolutions for resistive atmosphere setup. Although the spectra are noisy, a Kolmogorov like dependence is visible in both the setups.

7 CONCLUSIONS & DISCUSSIONS

In this paper we have presented the results of three dimensional MHD simulations of magnetic field configurations in NSs. We have considered both ideal MHD and a setup with a resistive atmosphere, and assume the field to be dipolar at the exterior boundary far from the star.

We have studied the evolution of both initially purely poloidal and mixed poloidal-toroidal fields with stronger toroidal components, and find that in all cases the initial configuration is unstable, with the instability developing on the order of an Alfvén crossing time scale. As the instability develops it gives rise to turbulence, and drives a small scale dynamo, which transfers helicity to the large scale field. The field attains a complex geometry with the toroidal component contributing $E_{\text{tor}} \leq 20\%$ of $E_{\text{m,tot}}$ in all setups, and while this is not a strict equilibrium, the ratio of the poloidal to toroidal energies in the field is approximately stable. The turbulence is not observed to decay during our simulations.

We find that stronger resistivity triggers the instability faster,

but does not impact its non-linear saturation, thus modifying only the timescales in our simulation. We also found that the extent of the atmosphere does not play any role in the overall equilibrium of the system, and the results do not change if we push the boundary of our simulation farther out, from 1.2 to 2 stellar radii.

Overall we find that a NS with a given inferred dipolar field strength far from the surface, is likely to harbour an interior toroidal component with an average energy of roughly 25% of the poloidal component, but that stronger toroidal fields are unstable and cannot be sustained. The overall geometry of the field is however complex, with higher multipoles growing closer to the surface, and moreover non-stationary over the life time of our simulations. We find rather a turbulent quasi-equilibrium, in which only average quantities are roughly constant. Further studies will focus on the decay of the turbulence and on quantifying the impact of these results on attempts to measure the mass and radius of a NS with X-ray observations from NICER, for which the background field configuration is an important ingredient (Bilous et al. 2019; Riley et al. 2019; Miller et al. 2019).

8 ACKNOWLEDGEMENT

We would like to thank Samuel Lander and Paul Lasky for useful comments and suggestions. AS gratefully acknowledges the help of Miljenko Cemeljic, Dipanjan Mukherjee and Varadarajan Parthasarathy for teaching PLUTO. AS further thanks Marco Antonelli for helping with the Kolmogorov spectrum. BH thanks Sebastiano Bernuzzi and David Hilditch for useful comments. This project was supported by an OPUS grant from the National Science Centre, Poland (NCN), number 2018/29/B/ST9/02013.

REFERENCES

Akgün T., Reisenegger A., Mastrano A., Marchant P., 2013, *MNRAS*, **433**, 2445

Armaza C., Reisenegger A., Alejand ro Valdivia J., 2015, *ApJ*, **802**, 121

Barrera R. G., Estevez G. A., Giraldo J., 1985, *European Journal of Physics*, **6**, 287

Bilous A. V., et al., 2019, *ApJ*, **887**, L23

Biskamp D., 2003, *Magnetohydrodynamic Turbulence*. Cambridge University Press, doi:10.1017/CBO9780511535222

Bocquet M., Bonazzola S., Gourgoulhon E., Novak J., 1995, *A&A*, **301**, 757

Braithwaite J., 2007, *Astron. Astrophys.*, **469**, 275

Braithwaite J., 2008, *MNRAS*, **386**, 1947

Braithwaite J., Nordlund A., 2006, *Astron. Astrophys.*, **450**, 1077

Braithwaite J., Spruit H. C., 2006, *Astron. Astrophys.*, **450**, 1097

Chandrasekhar S., Fermi E., 1953, *ApJ*, **118**, 116

Chung C. T. Y., Melatos A., 2011a, *MNRAS*, **411**, 2471

Chung C. T. Y., Melatos A., 2011b, *MNRAS*, **415**, 1703

Ciolfi R., Rezzolla L., 2012, *ApJ*, **760**, 1

Ciolfi R., Rezzolla L., 2013, *MNRAS*, **435**, L43

Ciolfi R., Ferrari V., Gualtieri L., 2010, *Mon. Not. Roy. Astron. Soc.*, **406**, 2540

Ciolfi R., Lander S. K., Manca G. M., Rezzolla L., 2011, *Astrophys. J.*, **736**, L6

Cutler C., 2002, *Phys. Rev. D*, **66**, 084025

Ferraro V. C. A., 1954, *ApJ*, **119**, 407

Flowers E., Ruderman M. A., 1977, *ApJ*, **215**, 302

Frederick S. G., Kuchera M. P., Thompson K. L., 2020

Frisch U., Pouquet A., LAL'Orat J., Mazure A., 1975, *Journal of Fluid Mechanics*, **68**, 769–778

Glampedakis K., Lasky P. D., 2015, *MNRAS*, **450**, 1638

Glampedakis K., Lasky P. D., 2016, *MNRAS*, **463**, 2542

Glampedakis K., Andersson N., Lander S. K., 2012, *MNRAS*, **420**, 1263

Goldreich P., Julian W. H., 1969, *ApJ*, **157**, 869

Güver T., Göğüş E., Özel F., 2011, *MNRAS*, **418**, 2773

Haskell B., Samuelsson L., Glampedakis K., Andersson N., 2008, *Mon. Not. Roy. Astron. Soc.*, **385**, 531

Herbrik M., Kokkotas K. D., 2017, *MNRAS*, **466**, 1330

Iroshnikov P. S., 1964, *Soviet Ast.*, **7**, 566

Kiuchi K., Yoshida S., 2008, *Phys. Rev. D*, **78**, 044045

Kolmogorov A., 1941, *Akademii Nauk SSSR Doklady*, **30**, 301

Kraichnan R. H., 1965, *The Physics of Fluids*, **8**, 1385

Lander S., Jones D., 2009, *Monthly Notices of the Royal Astronomical Society*, **395**, 2162

Lander S., Jones D., 2011, *Monthly Notices of the Royal Astronomical Society*, **412**, 1730

Lander S. K., Jones D. I., 2012, *MNRAS*, **424**, 482

Lander S. K., Jones D. I., 2018, *MNRAS*, **481**, 4169

Lander S. K., Jones D. I., 2019, arXiv e-prints, p. arXiv:1910.14336

Lander S., Jones D., Passamonti A., 2010, *Monthly Notices of the Royal Astronomical Society*, **405**, 318

Lasky P. D., 2015, *Publ. Astron. Soc. Australia*, **32**, e034

Lasky P. D., Melatos A., 2013, *Phys. Rev. D*, **88**, 103005

Lasky P. D., Zink B., Kokkotas K. D., Glampedakis K., 2011, *Astrophys. J.*, **735**, L20

Lasky P. D., Zink B., Kokkotas K. D., 2012

Lites B. W., et al., 2008, *ApJ*, **672**, 1237

Markey P., Tayler R. J., 1973, *MNRAS*, **163**, 77

Markey P., Tayler R. J., 1974, *MNRAS*, **168**, 505

Mignone A., Bodo G., Massaglia S., Matsakos T., Tesileanu O., Zanni C., 2007, *Astrophys. J. Suppl.*, **170**, 228

Miller M. C., et al., 2019, *ApJ*, **887**, L24

Mitchell J. P., Braithwaite J., Reisenegger A., Spruit H., Valdivia J. A., Langer N., 2015, *MNRAS*, **447**, 1213

Monaghan J. J., 1965, *MNRAS*, **131**, 105

Philippov A. A., Spitkovsky A., 2018, *ApJ*, **855**, 94

Pons J. A., Viganò D., 2019, *Living Reviews in Computational Astrophysics*, **5**, 3

Reisenegger A., 2009, *A&A*, **499**, 557

Riley T. E., et al., 2019, *ApJ*, **887**, L21

Roxburgh I. W., 1966, *MNRAS*, **132**, 347

Siegel D. M., Ciolfi R., Harte A. I., Rezzolla L., 2013, *Phys. Rev. D*, **87**, 121302

Spitkovsky A., 2006, *ApJ*, **648**, L51

Tayler R. J., 1957, *Proceedings of the Physical Society. Section B*, **70**, 31

Tayler R. J., 1973, *MNRAS*, **161**, 365

Thompson C., Duncan R. C., 1993, *ApJ*, **408**, 194

Thompson C., Duncan R. C., 1996, *The Astrophysical Journal*, **473**, 322

Wright G. A. E., 1973, *MNRAS*, **162**, 339

Zink B., Stergioulas N., Hawke I., Ott C. D., Schnetter E., Müller E., 2007, *Phys. Rev. D*, **76**, 024019

de Lima R. C. R., Coelho J. G., Pereira J. P., Rodrigues C. V., Rueda J. A., 2020, *ApJ*, **889**, 165